

## References and Notes

- S. Noda, *Science* **314**, 260 (2006).
- H. Altug, D. Englund, J. Vučković, *Nat. Phys.* **2**, 484 (2006).
- M. T. Hill, *J. Opt. Soc. Am. B* **27**, B36 (2010).
- K. J. Vahala, *Nature* **424**, 839 (2003).
- O. Painter *et al.*, *Science* **284**, 1819 (1999).
- A. Tandaechanurat *et al.*, *Nat. Photonics* **5**, 91 (2011).
- S. Strauf, F. Jahnke, *Laser Photon. Rev.* **5**, 607 (2011).
- W. L. Barnes, A. Dereux, T. W. Ebbesen, *Nature* **424**, 824 (2003).
- S. A. Maier, H. A. Atwater, *J. Appl. Phys.* **98**, 011101 (2005).
- D. K. Gramotnev, S. I. Bozhevolnyi, *Nat. Photonics* **4**, 83 (2010).
- J. A. Schuller *et al.*, *Nat. Mater.* **9**, 193 (2010).
- M. T. Hill *et al.*, *Nat. Photonics* **1**, 589 (2007).
- M. P. Nezhad *et al.*, *Nat. Photonics* **4**, 395 (2010).
- D. J. Bergman, M. I. Stockman, *Phys. Rev. Lett.* **90**, 027402 (2003).
- M. I. Stockman, *J. Opt.* **12**, 024004 (2010).
- M. A. Noginov *et al.*, *Nature* **460**, 1110 (2009).
- R. F. Oulton *et al.*, *Nature* **461**, 629 (2009).
- R.-M. Ma, R. F. Oulton, V. J. Sorger, G. Bartal, X. Zhang, *Nat. Mater.* **10**, 110 (2011).
- C.-Y. Wu *et al.*, *Nano Lett.* **11**, 4256 (2011).
- P. R. West *et al.*, *Laser Photon. Rev.* **4**, 795 (2010).
- P. Nagpal, N. C. Lindquist, S.-H. Oh, D. J. Norris, *Science* **325**, 594 (2009).
- J.-S. Huang *et al.*, *Nat. Commun.* **1**, 150 (2010).
- K. L. Shaklee, R. E. Nahory, R. F. Leheny, *J. Lumin.* **7**, 284 (1973).
- A. R. Smith, K.-J. Chao, Q. Niu, C. K. Shih, *Science* **273**, 226 (1996).
- H. Yu *et al.*, *Phys. Rev. Lett.* **88**, 016102 (2001).
- Information on methods, analyses, and simulations can be found in the supplementary materials available on Science Online.
- R. F. Oulton, V. J. Sorger, D. A. Genov, D. F. P. Pile, X. Zhang, *Nat. Photonics* **2**, 496 (2008).
- Y.-J. Lu, H.-W. Lin, H.-Y. Chen, Y.-C. Yang, S. Gwo, *Appl. Phys. Lett.* **98**, 233101 (2011).
- J. D. Jackson, *Classical Electrodynamics* (Wiley, New York, ed. 3, 1999), chap. 9.

**Acknowledgments:** We acknowledge support from the National Science Council in Taiwan (NSC-100-2120-M-007-001, NSC-98-2112-M-007-014-MY3, and NSC-98-2221-E-007-104-MY3) and, in the United States, the NSF (DMR-0906025, CMMI-0928664, and DGE-0549417), the Office of Naval Research (N00014-10-1-0929), the Air Force Office of Scientific Research (FA9550-08-1-0394), the Welch Foundation (F-1672), and the MOST of China (2009CB929102, 2012CB921302).

## Supplementary Materials

www.sciencemag.org/cgi/content/full/337/6093/450/DC1  
Materials and Methods  
Supplementary Text  
Figs. S1 to S7  
References (30–34)

18 April 2012; accepted 14 June 2012  
10.1126/science.1223504

# Predictive Self-Assembly of Polyhedra into Complex Structures

Pablo F. Damasceno,<sup>1\*</sup> Michael Engel,<sup>2\*</sup> Sharon C. Glotzer<sup>1,2,3†</sup>

Predicting structure from the attributes of a material's building blocks remains a challenge and central goal for materials science. Isolating the role of building block shape for self-assembly provides insight into the ordering of molecules and the crystallization of colloids, nanoparticles, proteins, and viruses. We investigated 145 convex polyhedra whose assembly arises solely from their anisotropic shape. Our results demonstrate a remarkably high propensity for thermodynamic self-assembly and structural diversity. We show that from simple measures of particle shape and local order in the fluid, the assembly of a given shape into a liquid crystal, plastic crystal, or crystal can be predicted.

The spontaneous organization of individual building blocks into ordered structures is ubiquitous in nature and found at all length scales. Examples include simple and complex crystals in atomic systems, liquid and plastic crystals in molecular materials, and superlattices of nanoparticles and colloids. Understanding the relation between building blocks and their assemblies is essential for materials design because physical properties depend intimately on structure. The formation of atomic materials structures can be rationalized, to first approximation, from geometric considerations (*1*), and with growing length scale, the shape of the building blocks becomes increasingly important. For colloidal particles interacting through the excluded volume arising from their shape (*2–5*), thermodynamic equilibrium structures ("phases") reported were relatively simple (*6–10*). The simulation prediction of a dodecagonal quasicrystal with tetrahedra (*11*) demonstrated the unexpected complexity that could be achieved for particles solely with hard interactions. Since then, ordered

structures have been reported for various polyhedra (*11–16*), which are now routinely synthesized as nanocrystals (*4, 5, 13, 17*). However, the a priori prediction of structure from particle shape has yet to be demonstrated.

The thermodynamic behavior of hard particles can be understood through entropy maximization (*18*). Packing efficiency plays an increasingly important role toward higher density and induces a preferential alignment of flat facets (*13, 19, 20*). Because packing efficiency increases with contact area, the alignment can be interpreted as the result of an effective, many-body directional entropic force (*14*) arising from the increased number of configurations available to the entire system, causing suitably faceted polyhedra to order. This notion of directional entropic forces and their relation to particle faceting suggests that particle shape can be used to predict assembled structures. To establish clear quantitative trends, however, requires data on many different shapes. We present thermodynamic Monte Carlo simulations of the self-assembly of 145 different polyhedra, including all the Platonic, Archimedean, Catalan, and Johnson solids and some zonohedra, prisms, and antiprisms, and we show that we can use particle shape to predict the general category of ordered structure that forms.

The polyhedra simulated, classified according to the structure(s) they assemble into from the dense fluid, are shown in Fig. 1. The names

of each polyhedron simulated and additional details can be found in fig. S1 and table S1 (*21*). We group polyhedra into three assembly categories (*12*): (i) crystals, (ii) plastic crystals, and (iii) liquid crystals. Polyhedra that are not observed to form ordered structures are grouped as (iv) disordered solids (glasses). The categories are further subdivided into classes based on the type of order and crystallographic symmetry. All structures reported form repeatedly from disordered fluid phases at packing fractions between 0.49 and 0.63, depending on particle shape. We first note that 101/145  $\approx$  70% of the polyhedra simulated assemble on the time scale of our simulations, which demonstrates a strong propensity for order in systems of polyhedra, even in the absence of explicit attractive interactions.

For crystals, we find five different Bravais lattices [hexagonal, cubic, body-centered tetragonal (BCT), rhombohedral, and orthorhombic]. The lattice shear we find with truncated cubes has been observed in experiments (*13, 22, 23*). The A5 lattice, graphite structure, honeycomb lattice, diamond structure (*14*), and "supercube" lattice are periodic and have only a few particles in the unit cell. The quasicrystals have been reported previously with tetrahedra (*11*) and triangular bipyramids (*24*). A new type of hexagonal random tiling forming independent layers is observed for the bilunabirotunda, a two-dimensional version of the random tiling seen in a molecular network (*25*).

Both the diversity and structural complexity possible with polyhedra are demonstrated by 12 representative structures. Four examples of crystals are analyzed in more detail. Dürer's solids form a simple cubic crystal (Fig. 2A), which is unusual because it is a degenerate crystal (*26*). Particles align randomly in four equivalent orientations. The space-filling gyrobifastigium assembles into a crystal isostructural to  $\beta$ -Sn, the metallic form of tin (Fig. 2B). Six square pyramids assemble into cubes ("supercubes") and then into a slightly sheared simple cubic lattice (Fig. 2C). The supercubes demonstrate the possibility of hierarchical

<sup>1</sup>Applied Physics Program, University of Michigan, Ann Arbor, MI 48109, USA. <sup>2</sup>Department of Chemical Engineering, University of Michigan, Ann Arbor, MI 48109, USA. <sup>3</sup>Department of Materials Science and Engineering, University of Michigan, Ann Arbor, MI 48109, USA.

\*These authors contributed equally to this work.

†To whom correspondence should be addressed. E-mail: sglotzer@umich.edu

assembly, similarly to a face-centered cubic (FCC) crystal reported for paired hemispheres (27). Pentagonal orthobicupola have a disklike shape and arrange with their five-fold symmetry axes aligned into the  $\beta$ -U crystal with the tiling (3.4.3<sup>2</sup>.4). A periodic approximant to a dodecagonal quasicrystal, this tiling is known as the sigma phase and has been observed in micelles (28, 29) and colloids (30), but with different decoration of the tiles (Fig. 2D).

We find that 66 of the 145 polyhedra crystallize into plastic crystals [rotator phases (31)] in which the particles are free to rotate about their lattice positions. The plastic crystals we find all correspond to the crystallographically dense packings FCC (or hexagonally close-packed, HCP), body-centered cubic (BCC), and three topologically close-packed (TCP) polytetrahedral structures isostructural to  $\beta$ -W,  $\beta$ -Mn, and  $\gamma$ -brass. We do not distinguish between FCC and HCP, because simulations of these structures often contain high densities of stacking faults. In a TCP structure, lattice sites are coordinated by distorted tetrahedra. We always observe plastic crystals for these three types of crystals.

In Fig. 2E, we show that rhombic dodecahedra (the Voronoi cell of FCC) order into an FCC plastic crystal. We observe that the plastic crystal transforms into a nonrotator phase at higher packing fractions. Elongated triangular cupolas assemble a plastic BCC crystal (Fig. 2F). The formation of a high-symmetry phase is counterintuitive given the asymmetric shape of the cupola. The paradigmatic rhombicosidodecahedron has two large parallel faces and forms a plastic TCP phase isostructural to  $\beta$ -W (Fig. 2G). This phase, also known as the A15 structure, is frequently observed with micelles (32). Dodecahedra assemble into the complex  $\beta$ -Mn structure (Fig. 2H). Because the distribution of Bragg peaks in the diffraction pattern resembles eight-fold symmetry,  $\beta$ -Mn can be interpreted as an approximant of an octagonal quasicrystal (33). Indeed, we often observe eight-fold symmetry in the diffraction pattern during intermediate stages of crystallization. Truncated dodecahedra form  $\gamma$ -brass (Fig. 2I). With 52 atoms per unit cell, it is the most complex periodic crystal observed in this study.

A nematic liquid crystal is formed by the pentagonal pyramid, which has a plateletlike shape (Fig. 2J). The up-down orientation of the pyramid relative to the director is random. The elongated square pyramid assembles into smectic layers (Fig. 2K). We confirmed that there is no preferred orientation or long-range translational order within the layers. Like all regular prisms and antiprisms with five-fold or higher symmetry, the pentagonal prism assembles a columnar phase (34). Particles are free to both shift along and rotate around the column axis (Fig. 2L).

Forty-four polyhedra never self-assemble into an ordered structure on the time scale of our simulations, despite run times more than an order of magnitude longer than that needed for the slowest formation of a crystal. Instead, the par-

ticle dynamics becomes gradually slower with increasing packing fraction, which eventually produces a glassy state without discernible rotational or translational order. Because studies of dense packings of these polyhedra (34) yield crystals with higher packing fractions, we expect that the 44 particles have ordered "ground states" in the limit of infinite pressure. As in other examples (11, 24), those ordered states may not be kinetically accessible in experiments. It is interesting to note that 41 of the 44 that form glasses are Johnson solids, and most are not centrally symmetric. Johnson solids are typically less symmetric than Platonic and Archimedean solids, which all order in our simulations. This agrees with the intuition that highly symmetric polyhedra might be more easily assembled than nonsymmetric ones. A complete investigation of assembly kinetics and propensity requires a careful analysis of the equations of state (10, 15, 24, 35). Preliminary data suggest that particles from the same assembly category have a comparable entropy gain  $\Delta S$  at the transition. For instance, liquid crystals have  $\Delta S = (1.8 \pm 0.5)k_B$  and plastic crystals,  $\Delta S = (1.0 \pm 0.5)k_B$ , where  $k_B$  is the Boltzmann constant. No clear trend is observed for shapes that assemble into crystals.

Several parameters have been used in the literature to analyze the shape of polyhedra (12, 19, 34). A parameter that is sufficiently sensitive to large shape changes, but not too sensitive to small deformations, is the isoperimetric quotient, defined as  $IQ = 36\pi V^2/S^3$ , where  $V$  is volume and  $S$  is surface area (36, 37). IQ can be calculated easily from the vertex vectors and is closely related to the shape factor used in equations of state of hard convex bodies (38). A second parameter, the coordination number  $CN_f$ , accounts for the local arrangement of particles in the fluid phase before crystallization. In the case of glasses, we measure the coordination number at packing fraction 55%, which is the packing fraction where we typically observe crystallization of polyhedra that do not form glasses.

A correlation between the parameters IQ and  $CN_f$  and the assembly categories of Fig. 1 can be seen in Fig. 3A. We divide the parameter space into three regions. In the rightmost region ( $IQ > 0.7$ ), 58 of 59 highly spherical polyhedra are observed to form plastic crystals. In the bottom-most region ( $CN_f < 2$ ), 21 of 24 polyhedra with few neighbors form liquid crystals. Finally, 16 of 18 particles in the center region ( $IQ \leq 0.7$  and  $CN_f \geq 2$ ) assemble into crystals. Thus, based on

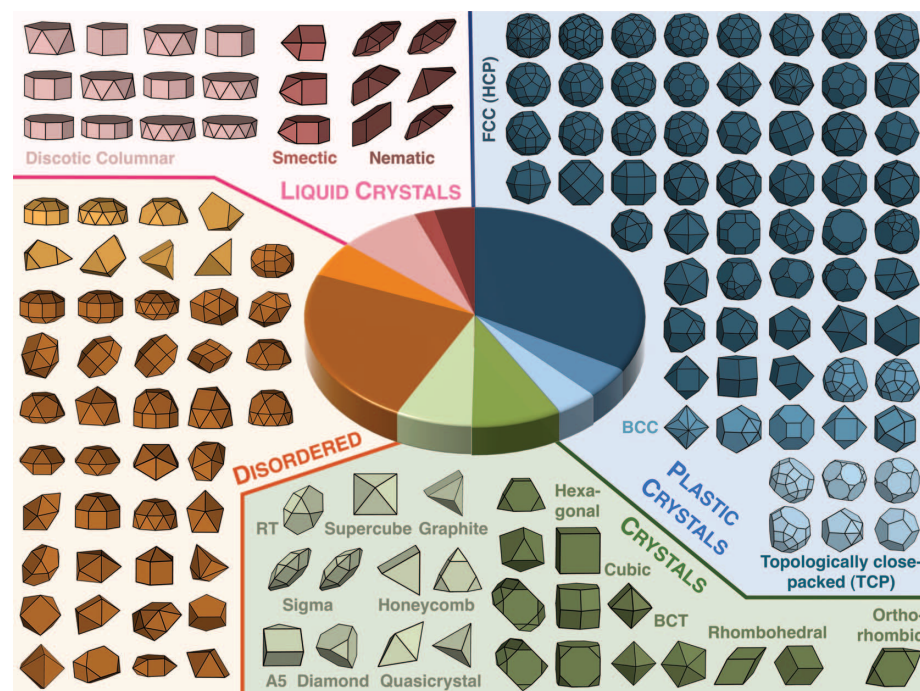


**Fig. 1.** Polyhedra are separated into four categories of organization as indicated by different colors: liquid crystals, plastic crystals, crystals, and disordered (glassy) phases. Subcategories (classes) are indicated by shades. The assembly category of liquid crystals contains the classes discotic columnar, smectic, and nematic (different shades of pink). Plastic crystal classes are FCC (dark blue), BCC (blue), and TCP (light blue). In the case of crystals, we distinguish Bravais lattices (dark green) and non-Bravais lattices (light green). RT stands for random tiling. For the glasses, no assembly is observed, and we distinguish those that strongly order locally with preferential face-to-face alignment (light orange) from those with only weak local order (dark orange). The pie chart in the center compares the relative frequency of the 10 observed classes. In each of the classes, polyhedra are listed in decreasing order of the isoperimetric quotient. A polyhedron is included multiple times if it was found to assemble into more than one ordered structure.



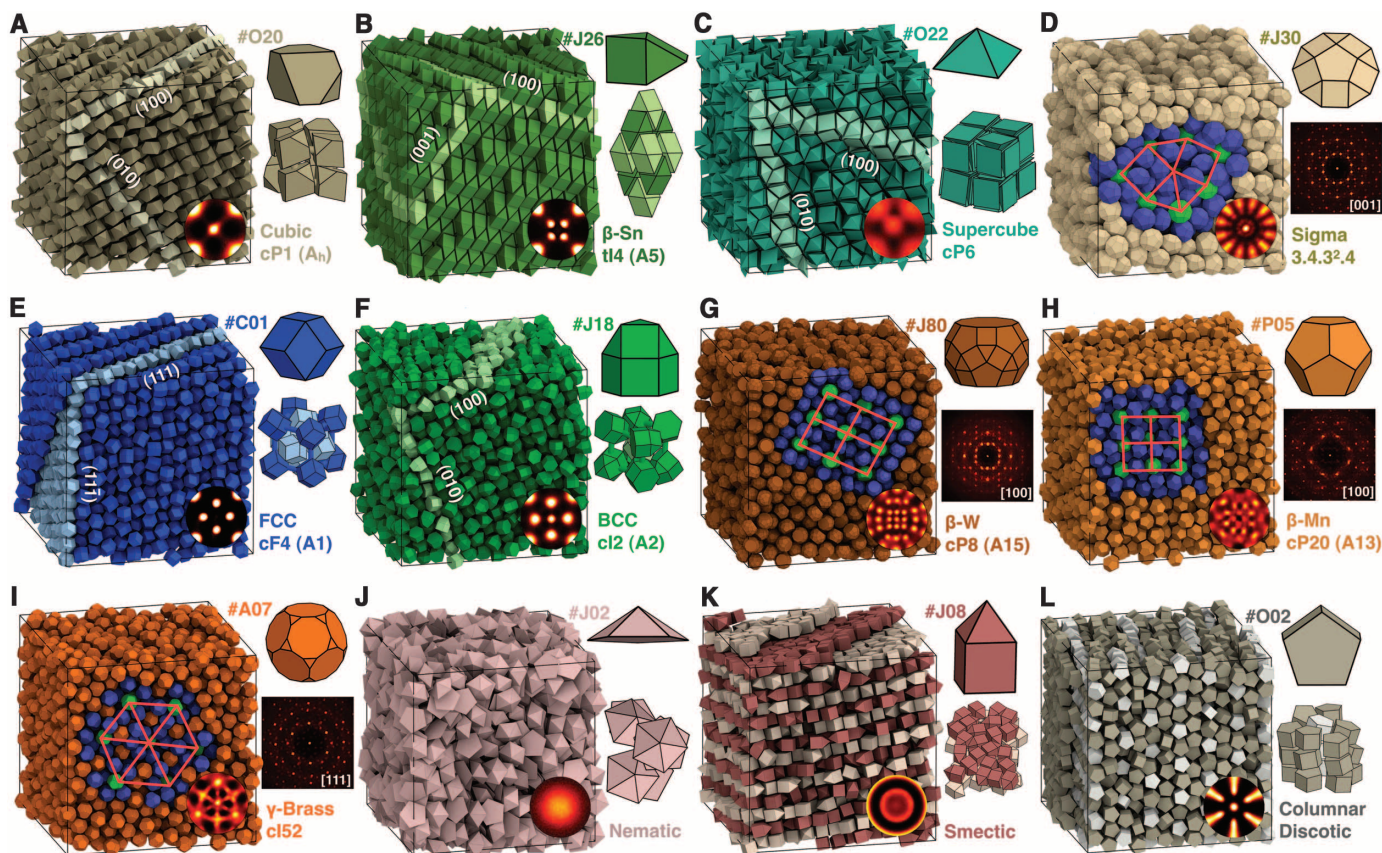


**Fig. 2.** Systems of 2048 polyhedra were assembled starting from the disordered fluid. In each subfigure, a snapshot of the simulation box (left), the bond-order diagram for nearest neighbors (inset), the polyhedron shape and ID (top right), a small group of particles or the diffraction pattern (middle right), and the crystallographic characterization consisting of name or atomic proto-

type, Pearson symbol, and Strukturbericht designation (bottom right) are shown. The snapshots depict crystals (A to D), plastic crystals (E to I), and liquid crystals (J to L). Some low index planes (A to C, E, and F), tiling descriptions consisting of squares and triangles (D and G to I) and structural features (K and L) are highlighted in the simulation snapshots by different colors.

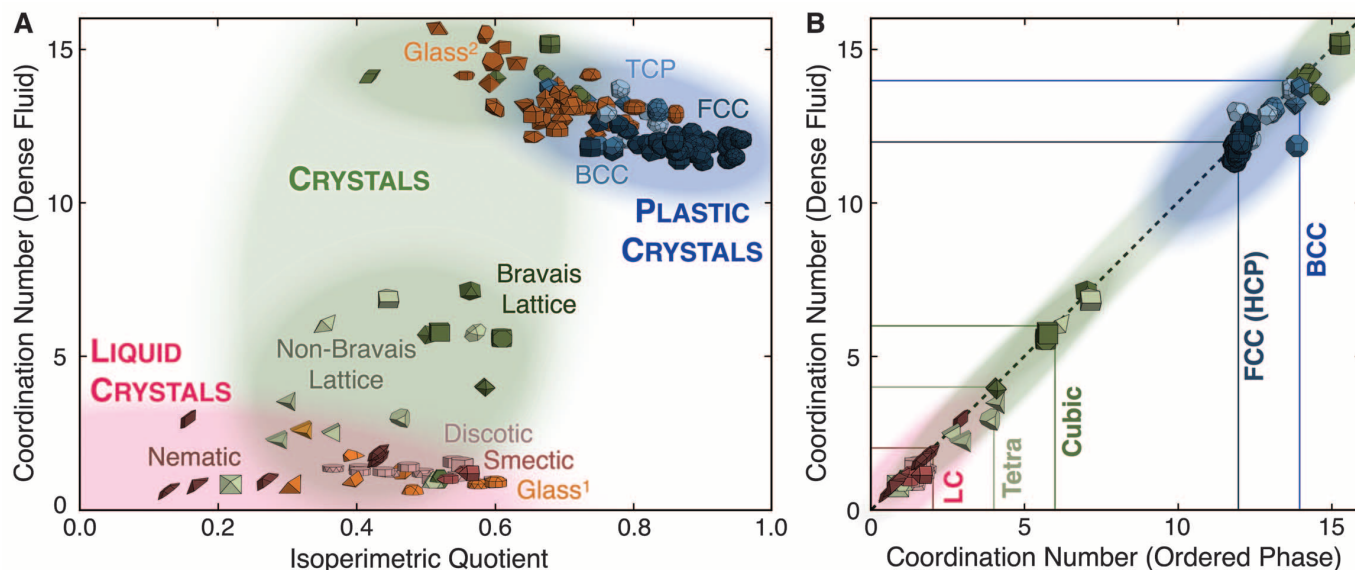


**Fig. 3.** (A) The coordination number in the fluid phase,  $CN_f$ , is correlated to the isoperimetric quotient (IQ) of the polyhedron. Here, IQ is a scalar parameter for the sphericity of the shape and coordination number is a measure for the degree of local order. Data points are drawn as small polyhedra. Polyhedra are colored and grouped according to the assem-

blies they form. (B) Polyhedra have, in most cases, nearly identical coordination number in the ordered phase ( $CN_o$ ) and the fluid phase ( $CN_f$ ) close to the ordering transition. Because of this strong correlation, combining  $CN_f$  and IQ allows for prediction of the assembly category expected for most cases.



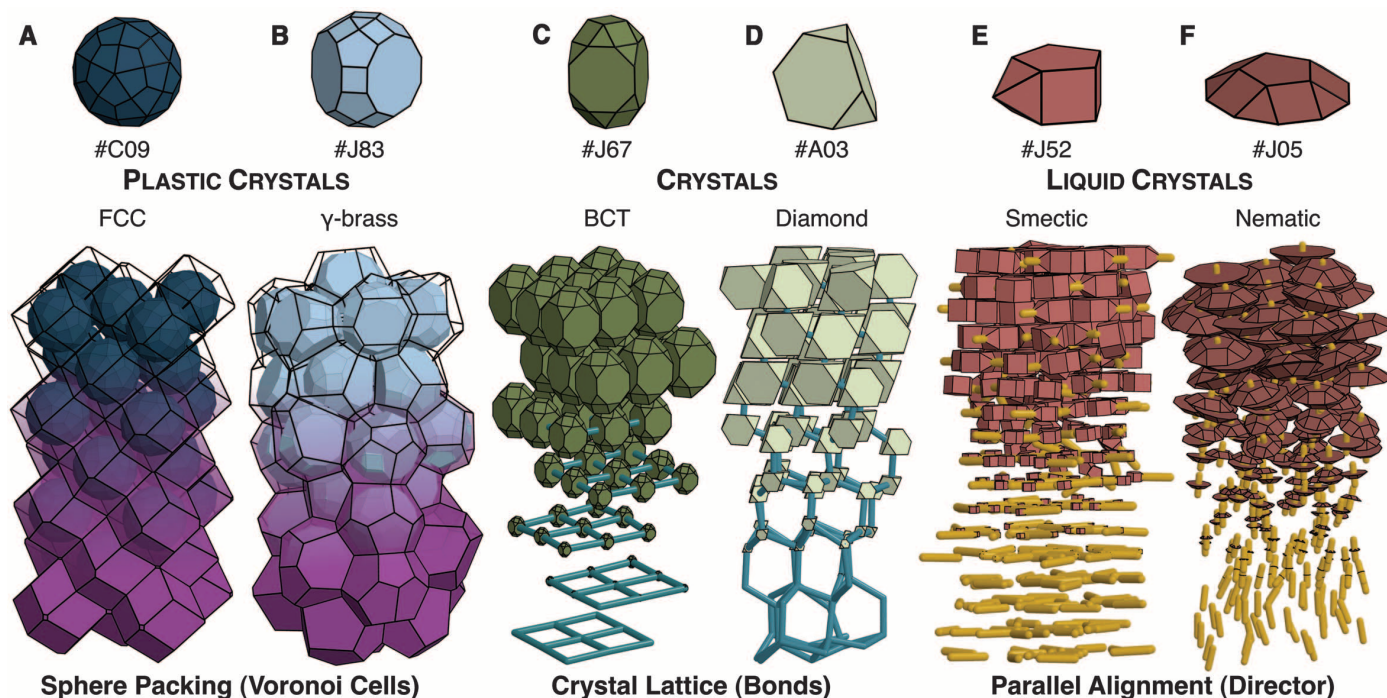


**Fig. 4.** We analyze six systems of polyhedra that span the three assembly categories observed with hard polyhedra. Polyhedra and their IDs are shown at top and small groups of particles are extracted from simulation snapshots below. (A and B) In plastic crystals, polyhedra rotate inside their Voronoi cells.

(C and D) Entropic “bonds” in the direction of the face normal are important for crystals. (E and F) Parallel alignment dominates in the case of liquid crystals. From top to bottom, the transparency of Voronoi cells is decreased and/or the size of polyhedra is reduced.

IQ and  $CN_f$  alone, the assembly of  $95/101 = 94\%$  of the polyhedra studied into crystals, liquid crystals, or plastic crystals is predicted. The outliers either lie within boundaries between regions, or they are nearly space-filling, which favors crystals over liquid or plastic crystals. We expect the shaded regions in Fig. 3A to become further refined as additional shapes are investigated. For example, the liquid crystal region is expected to expand upward for prolate particles (not studied here), which have a higher  $CN_f$  than oblate particles yet still have a low IQ.

We compare the coordination number measured close to the ordering transition in the fluid ( $CN_f$ ) and in the ordered structure ( $CN_o$ ) in Fig. 3B. Both numbers are nearly identical for almost all 101 shapes that assemble. This explains why it is sufficient to determine the coordination number in the dense fluid, which can be obtained from short simulations and experiments by integrating over the first peak of the radial distribution function, to predict with reasonable accuracy the category of structure that will form from the disordered fluid. As an independent test of Fig. 3A, we calculated the IQ and  $CN_f$  for the family of truncated tetrahedra studied in (14) and correctly predict that each member should form a crystal (fig. S2).

When comparing our observations with known crystal structures of atoms and molecules, which can be rationalized in terms of a few parameters, like the strength and directionality of bonds between atoms (39) and the molecular geometry (40),

we can interpret our findings as follows. First, FCC (HCP) and BCC crystals form from highly spherical polyhedra that have nondirectional or weakly directional entropic interactions. TCP structures are a compromise between high density and maintaining icosahedral local order present in the dense liquid. The coordination geometry can be visualized with Voronoi cells (Fig. 4, A and B). Voronoi cells of TCP structures often have pentagonal or hexagonal faces. We frequently find TCP structures with particles that resemble the Voronoi cells, such as the (truncated) dodecahedron. The assembly of plastic crystals is dominated by packing, and their atomic analog is metals and metallic bonding. It is interesting to note that all of our plastic crystals except  $\gamma$ -brass are isostructural to crystals found in elementary metals. Second, polyhedra that form crystals are more aspherical, with more pronounced and fewer faces. The crystal lattice is well represented by an ordered network of entropic “bonds” (Fig. 4, C and D). Polyhedra assembling into crystals do not always resemble the Voronoi cells of the crystal, but usually have strong directional entropic bonding, reminiscent of covalent bonds. Third, polyhedra forming liquid crystals typically have an axial shape. Alignment of the most prominent faces is important for these phases and can be analyzed by the alignment of the directors (Fig. 4, E and F). In general, we expect for axial particles to align prominent faces and long particle dimensions first. The behavior of polyhedra forming liquid crystals corresponds most closely to mo-

lecular liquid crystals. In all cases, the degree of directional entropic bonding may be quantified through various shape descriptors and correlation functions (fig. S3).

Our results push the envelope of entropic crystallization and the assembly behavior of hard particle fluids and provide an important step toward a predictive science of nanoparticle and colloidal assembly, which will be necessary to guide experiments with families of polyhedrally shaped particles that are now becoming available. Although we are not yet able to predict a specific structure (e.g., BCC or diamond), the knowledge that obtaining, e.g., the diamond structure requires a shape with intermediate IQ or that a complex, topologically close-packed structure like  $\gamma$ -brass requires a shape with high IQ provides important predictive guidance for building block design and synthesis. With further developments, more refined future structure prediction, with the level of detail now possible for atoms (41), should be attainable.

#### References and Notes

1. L. Pauling, *J. Am. Chem. Soc.* **51**, 1010 (1929).
2. F. Li, D. P. Josephson, A. Stein, *Angew. Chem. Int. Ed.* **50**, 360 (2011).
3. S. C. Glotzer, M. J. Solomon, *Nat. Mater.* **6**, 557 (2007).
4. Z. Quan, J. Fang, *Nano Today* **5**, 390 (2010).
5. M. H. Huang, P.-H. Lin, *Adv. Funct. Mater.* **22**, 14 (2012).
6. B. J. Alder, T. E. Wainwright, *J. Chem. Phys.* **27**, 1208 (1957).
7. M. D. Eldridge, P. A. Madden, D. Frenkel, *Nature* **365**, 35 (1993).
8. L. Onsager, *Ann. N.Y. Acad. Sci.* **51**, 627 (1949).

9. D. Frenkel, H. N. W. Lekkerkerker, A. Stroobants, *Nature* **332**, 822 (1988).
10. D. Frenkel, B. M. Mulder, *Mol. Phys.* **55**, 1171 (1985).
11. A. Haji-Akbari et al., *Nature* **462**, 773 (2009).
12. U. Agarwal, F. A. Escobedo, *Nat. Mater.* **10**, 230 (2011).
13. J. Henzie, M. Grünwald, A. Widmer-Cooper, P. L. Geissler, P. Yang, *Nat. Mater.* **11**, 131 (2011).
14. P. F. Damasceno, M. Engel, S. C. Glotzer, *ACS Nano* **6**, 609 (2012).
15. R. Ni, A. P. Gantapara, J. de Graaf, R. van Roij, M. Dijkstra, <http://dx.doi.org/10.1039/C2SM25813G>.
16. F. Smalenburg, L. Filion, M. Marechal, M. Dijkstra, <http://arXiv.org/abs/1111.3466>.
17. L. Rossi et al., *Soft Matter* **7**, 4139 (2011).
18. D. Frenkel, *Physica A* **263**, 26 (1999).
19. S. Torquato, Y. Jiao, *Nature* **460**, 876 (2009).
20. K. L. Young et al., *Proc. Natl. Acad. Sci. U.S.A.* **109**, 2240 (2012).
21. Materials and methods are available as supplementary materials on Science Online.
22. K. Zhao, R. Bruinsma, T. G. Mason, *Proc. Natl. Acad. Sci. U.S.A.* **108**, 2684 (2011).
23. Y. Zhang, F. Lu, D. van der Lelie, O. Gang, *Phys. Rev. Lett.* **107**, 135701 (2011).
24. A. Haji-Akbari, M. Engel, S. C. Glotzer, *Phys. Rev. Lett.* **107**, 215702 (2011).
25. M. O. Blunt et al., *Science* **322**, 1077 (2008).
26. S. J. Gerbode, S. H. Lee, C. M. Liddell, I. Cohen, *Phys. Rev. Lett.* **101**, 058302 (2008).
27. M. Marechal, R. J. Kortschot, A. F. Demirörs, A. Imhof, M. Dijkstra, *Nano Lett.* **10**, 1907 (2010).
28. G. Ungar, Y. Liu, X. Zeng, V. Percec, W.-D. Cho, *Science* **299**, 1208 (2003).
29. S. Lee, M. J. Bluemle, F. S. Bates, *Science* **330**, 349 (2010).
30. D. V. Talapin et al., *Nature* **461**, 964 (2009).
31. Although "rotator phases" constitute a subset of "plastic crystals" in molecular materials, the terms are used synonymously for hard particles.
32. P. Zihler, R. D. Kamien, *J. Phys. Chem. B* **105**, 10147 (2001).
33. M. Elenius, F. Zetterling, M. Dzugutov, D. Fredrickson, S. Lidin, *Phys. Rev. B* **79**, 144201 (2009).
34. J. de Graaf, R. van Roij, M. Dijkstra, *Phys. Rev. Lett.* **107**, 155501 (2011).
35. A. Haji-Akbari, M. Engel, S. C. Glotzer, *J. Chem. Phys.* **135**, 194101 (2011).
36. G. Poly, *Induction and Analogy in Mathematics* (Princeton Univ. Press, Princeton, NJ, 1954), pp. 188–189.
37. W. L. Miller, A. Cacciuto, *J. Chem. Phys.* **133**, 234903 (2010).
38. I. Nezbeda, *Chem. Phys. Lett.* **41**, 55 (1976).
39. G. S. Rohrer, *Structure and Bonding in Crystalline Materials* (Cambridge Univ. Press, Cambridge, 2004).
40. J. N. Israelachvili, *Intermolecular and Surface Forces* (Academic Press, Waltham, MA, 2010), pp. 535–576.
41. S. M. Woodley, R. Catlow, *Nat. Mater.* **7**, 937 (2008).

**Acknowledgments:** This material is based in part upon work supported by the Assistant Secretary of Defense for Research and Engineering, U.S. Department of Defense [DOD/ASD(R&E)] (N00244-09-1-0062). Any opinions, findings, and conclusions or recommendations expressed in this publication are those of the authors and do not necessarily reflect the views of the DOD/ASD(R&E). S.C.G. acknowledges support by the U.S. Army Research Office under Grant Award no. W911NF-10-1-0518. M.E. acknowledges support from the Deutsche Forschungsgemeinschaft (EN 905-1/1). P.F.D. was supported in part by the U.S. Air Force Office of Scientific Research under Multidisciplinary University Research Initiative no. FA9550-06-1-0337, subaward no. 444286-P061716. We thank R. G. Petschek and J. M. Millunchick for comments on the original manuscript.

#### Supplementary Materials

[www.sciencemag.org/cgi/content/full/337/6093/453/DC1](http://www.sciencemag.org/cgi/content/full/337/6093/453/DC1)  
Materials and Methods  
Supplementary Text  
Figs. S1 to S3  
Table S1  
References (42, 43)

21 February 2012; accepted 11 June 2012  
10.1126/science.1220869

## The Tides of Titan

Luciano Iess,<sup>1\*</sup> Robert A. Jacobson,<sup>2</sup> Marco Ducci,<sup>1</sup> David J. Stevenson,<sup>3</sup> Jonathan I. Lunine,<sup>4</sup> John W. Armstrong,<sup>2</sup> Sami W. Asmar,<sup>2</sup> Paolo Racioppa,<sup>1</sup> Nicole J. Rappaport,<sup>2</sup> Paolo Tortora<sup>5</sup>

We have detected in Cassini spacecraft data the signature of the periodic tidal stresses within Titan, driven by the eccentricity ( $e = 0.028$ ) of its 16-day orbit around Saturn. Precise measurements of the acceleration of Cassini during six close flybys between 2006 and 2011 have revealed that Titan responds to the variable tidal field exerted by Saturn with periodic changes of its quadrupole gravity, at about 4% of the static value. Two independent determinations of the corresponding degree-2 Love number yield  $k_2 = 0.589 \pm 0.150$  and  $k_2 = 0.637 \pm 0.224$  ( $2\sigma$ ). Such a large response to the tidal field requires that Titan's interior be deformable over time scales of the orbital period, in a way that is consistent with a global ocean at depth.

Since its gravitational capture by Saturn on 1 July 2004, the spacecraft Cassini has flown by Titan more than 80 times, carrying out extensive observations of the surface and the atmosphere by means of particle and remote sensing instruments. In contrast, information on the moon's deep interior is scarce. Lacking a detectable internally generated magnetic field, constraints on the interior of Titan come from gravity, topography, and rotation measurements. Titan's main deviations from spherical symmetry are caused by centrifugal and tidal forces, associated respectively with the rotation about its spin axis and the gradient of Saturn's gravity. The moon responds to the centrifugal and tidal potentials

with deformations that (to the lowest order) change its quadrupole field. In a body-fixed frame with the prime meridian pointing to the central planet at pericenter and the  $z$  axis along the instantaneous rotation axis (coinciding with the orbit normal), only the  $J_2$  and  $C_{22}$  quadrupole coefficients are different from zero for a relaxed, synchronous satellite. They are bound by the constraint  $J_2/C_{22} = 10/3$ . The satellite's static response to the external fields is usually characterized by a single parameter, the fluid Love number  $k_F$ , which reaches its maximum value of  $3/2$  for an incompressible fluid body. Previous determinations of Titan's gravity ( $I$ ) yielded  $k_F = 1.0097 \pm 0.0039$ , implying a relaxed shape, very close to hydrostatic equilibrium. The value smaller than  $3/2$  revealed a significant concentration toward the center, with a moment of inertia factor  $\tilde{C} = 0.3414 \pm 0.0005$  (inferred from the Radau-Darwin equation). However, the non-negligible eccentricity of Titan's orbit causes a variation with time of the quadrupole tidal field [proportional to  $1/r^3$  ( $r$ , distance between Titan and the Saturn barycenter)]. These short-term variations change the satellite's physical shape

and gravity. Titan's linear response to the periodic tidal field entails a corresponding periodic change in its own quadrupole potential. The ratio between the perturbed and the perturbing potentials is known as the  $k_2$  Love number. It is an indication of the mass redistribution inside the body in response to the forcing potential.  $k_2$ , like  $k_F$ , reaches its theoretical upper limit of  $3/2$  for an incompressible liquid body, whereas for a perfectly rigid body,  $k_2 = 0$ . If Titan hosts a global subsurface ocean, then  $k_2$  must differ substantially from zero. We have detected the signature of the tidal forcing in Cassini data and derived a value of  $k_2$ .

Our observational strategy entailed gravity determinations near the pericenter and apocenter of Titan's orbit. For  $k_2 = 0.4$  (a typical value if an ocean is present), the expected peak-to-peak variations of the quadrupole coefficients are about 4% for  $J_2$  and 7% for  $C_{22}$  (2, 3). The corresponding change in the spacecraft acceleration, about 0.2 mgal in the most favorable geometry, is measurable by the Cassini tracking

**Table 1.** Titan's  $k_2$  Love number, estimated from different data analysis procedures (supplementary materials) and representations of the gravity field: multi-arc analysis and  $3 \times 3$  gravity field (SOL1a); multi-arc analysis and  $4 \times 4$  gravity field (SOL1b); and global solution with  $3 \times 3$  gravity field (SOL2). SOL1 and SOL2 were produced independently by the Cassini Radio Science Team and the Navigation Team.

	$k_2$ (value $\pm 1\sigma$ )		
SOL1a	0.589	$\pm$	0.075
SOL1b	0.670	$\pm$	0.090
SOL2	0.637	$\pm$	0.112

<sup>1</sup>Dipartimento di Ingegneria Meccanica e Aerospaziale, Università La Sapienza, via Eudossiana 18, 00184 Rome, Italy. <sup>2</sup>Jet Propulsion Laboratory, 4800 Oak Grove Drive, Pasadena, CA 91109, USA. <sup>3</sup>Division of Geological and Planetary Sciences, California Institute of Technology, Pasadena, CA 91125, USA. <sup>4</sup>Department of Astronomy, Cornell University, Ithaca, NY 14850, USA. <sup>5</sup>DIEM-II Facoltà di Ingegneria, Università di Bologna, I-47121 Forlì, Italy.

\*To whom correspondence should be addressed. E-mail: [luciano.iess@uniroma1.it](mailto:luciano.iess@uniroma1.it)